Conversion of Bilayers of PS-*b*-PDMS Block Copolymer into Closely Packed, Aligned Silica Nanopatterns

Nathanael L. Y. Wu,[†,‡] Kenneth D. Harris,[†,*] and Jillian M. Buriak[†,§,*]

[†]National Institute for Nanotechnology (NINT), National Research Council, 11421 Saskatchewan Drive, Edmonton, Alberta T6G 2M9, Canada, [‡]Department of Electrical and Computer Engineering, University of Alberta, Edmonton, Alberta T6G 2G8, Canada, and [§]Department of Chemistry, University of Alberta, Edmonton, Alberta T6G 2G2, Canada

ABSTRACT Block copolymer (BCP) self-assembly is an effective and versatile approach for the production of complex nanopatterned interfaces. Monolayers of BCP films can be harnessed to produce a variety of different patterns, including lines, with specific spacings and order. In this work, bilayers of cylinder-forming polystyrene-*block*-polydimethylsiloxane block copolymer (PS-*b*-PDMS) were transformed into arrays of silica lines with half the pitch normally attained for conventional monolayers, with the PDMS acting as the source for the SiO_x. The primary hurdle was ensuring the bilayer silica lines were distinctly separate; to attain the control necessary to prevent overlap, a number of variables related to the materials and self-assembly process were investigated in detail. Developing a detailed understanding of BCP film swelling during solvent annealing, blending of the PS-*b*-PDMS with PS homopolymer, utilization of a surface brush layer, and adjustment of the plasma exposure conditions, distinct and separate silica lines were prepared. On the microscale, the sample coverage of PS-*b*-PDMS bilayers was investigated and maximized to attain >95% bilayers under defined conditions. The bilayer BCP structures were also amenable to graphoepitaxy, and thus, dense and highly ordered arrays of silica line patterns with tightly controlled width and pitch were fabricated and distributed uniformly across a Si surface.

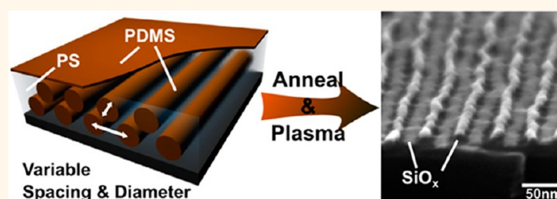

KEYWORDS: block copolymer · brush layer · graphoepitaxy · homopolymer blends · patterning · plasma · PS-*b*-PDMS · self-assembly · solvent annealing

The self-assembly of block copolymers (BCPs) into ordered arrays of nanostructures on surfaces with sparing outside intervention has stimulated a great deal of interest.[1−8] Through careful polymer design, the size, spacing and morphology of the resulting self-assembled BCP features can be tuned to any size on the order of tens of nanometers.[9−14] For a given BCP, varying the processing conditions (such as using thermal or solvent annealing, initial thicknesses, *etc.*) will also allow for finer control of the nanopattern size and morphology.[15,16] Due to a combination of thermodynamic and kinetic factors involved in the self-assembly process,[17] there are, however, limitations for a given neat BCP of composition A-B to form assemblies with critical dimensions smaller or larger than its "natural" value. With the increasing focus on the production of sub-20 nm features,[10,13,18−20] approaches to induce a given BCP system to form smaller structures than would normally be possible under standard equilibrium conditions are valuable.

From an applications standpoint, BCPs have many potential uses, including lithographic templates for data storage and memory,[21−24] integrated circuits,[25] contact holes,[26,27] and tissue interfacing.[28,29] As has been described within the International Technology Roadmap for Semiconductors (ITRS), BCPs have demonstrated the capability to form the palette of patterns required for integrated circuit production within short periods of time.[30−32] Highly ordered, self-assembled BCP patterns that differ from their typical equilibrium nanostructures can also be produced through ordered templates or directed self-assembly. Many examples of directed self-assembly to produce diverse, highly complex structures relevant to device manufacturing have been demonstrated in the past decade. For example, BCPs have been driven to self-assemble into bends (acute and obtuse),[33]

* Address correspondence to jburiak@ualberta.ca, ken.harris@nrc-cnrc.gc.ca.

Received for review April 19, 2013 and accepted May 11, 2013.

Published online May 12, 2013
10.1021/nn401968t

© 2013 American Chemical Society

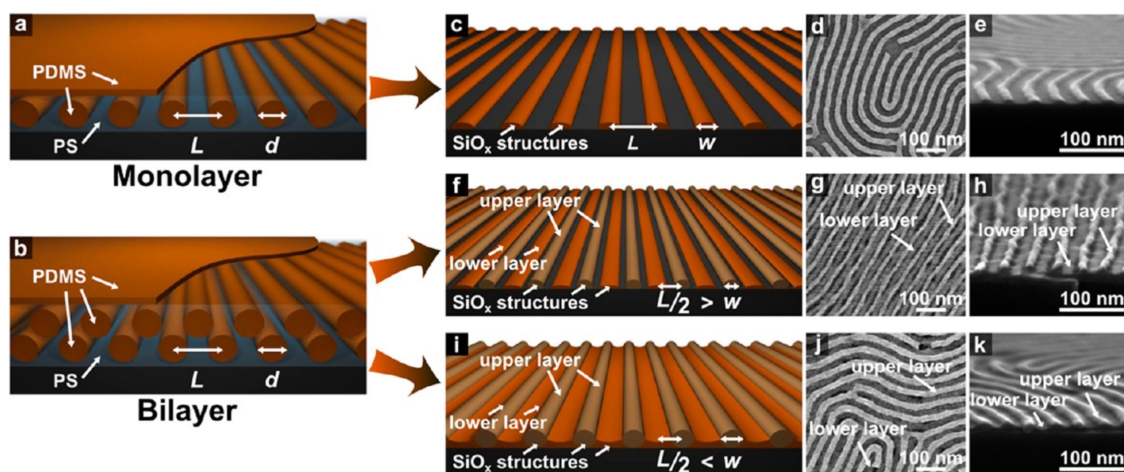

Figure 1. **(a and b) Schematics of self-assembled PS-*b*-PDMS monolayer (a) and bilayer (b) films after solvent vapor annealing: horizontal cylindrical PDMS structures (characteristic spacing *L* and cylinder width *d*) are surrounded by a PS matrix and a thin PDMS surface layer. After plasma treatment, these cylindrical structures become line patterns that are clearly visible in the plan view and cross section SEM images to the right. (c−e) Lines patterned from monolayers of PDMS cylinders have line pitch *L* and line width *w*. (f−h) Ideal lines patterned from PS-*b*-PDMS bilayers are separated and have line pitch *L*/2 and line width $w < L/2$. (i−k) Lines are not neatly separated and may overlap when $w > L/2$.**

jogs,[34] isolated segments,[34] T- and Y-junctions,[35] checkerboards,[36] and rectangular trimming patterns[36] through chemical prepatterning of the substrate surface. By utilizing graphoepitaxy and predefined topographical features prepared *via* electron beam lithography, selectively and locally complex linear patterns[37] or cross-hatched patterns[38] can also be formed. For future scale-up, reducing the spatial frequency of the topographic features that assist in directing the self-assembly is an attractive goal. One of the most demanding metrics outlined in the ITRS Roadmap, however, focuses on the size and spacing of the self-assembled BCP features. Beautiful work to reduce feature sizes has been accomplished by increasing the Flory−Huggins separation parameter[18,19] or by using cyclic copolymers with their small hydrodynamic radii.[12]

In this work, we show how self-assembled bilayers of polystyrene-*block*-polydimethylsiloxane (PS-*b*-PDMS) horizontal cylindrical structures can be harnessed to generate closely spaced silica (SiO_x) lines on surfaces, as outlined in Figure 1. Monolayers and bilayers of self-assembled PS-*b*-PDMS cylinders were converted into silica lines with pitches of *L* and *L*/2, respectively. Control over the dimensions of the resulting silica lines, including line width and pitch, is demonstrated through tailoring of surface brush layers, polymer film composition, annealing conditions and plasma etch parameters. In earlier work, we showed how self-assembled bilayers of polystyrene-*block*-poly-(2-vinylpyridine) (PS-*b*-P2VP) could be metallized and then converted into density-doubled lines,[39] but with PS-*b*-PDMS, the metallization step is avoided since the intrinsic PDMS block is directly converted into SiO_x. More importantly, we anticipated that the high Flory−Huggins interaction parameter of PS-*b*-PDMS ($\chi_{PS\text{-}b\text{-}PDMS} = 0.27$[40] compared to $\chi_{PS\text{-}b\text{-}P2VP} = 0.18$[41] at room temperature) would enable the formation of finer structures with lower line edge roughness.[9,18] Because silica is a ubiquitous material to which a wide range of molecules, nanoparticles and other functionalities can be covalently connected,[42−45] these SiO_x nanopatterns could provide a pathway for the generation of complex hierarchical assemblies.

RESULTS AND DISCUSSION

A PS-*b*-PDMS BCP with $M_{n(PS)} = 31.0$ kg/mol and $M_{n(PDMS)} = 14.5$ kg/mol was used for all the experiments described here, and the as-cast PS-*b*-PDMS films were solvent annealed in tetrahydrofuran (THF) vapor to promote self-assembly into ordered cylinder arrays. Generally, regions with monolayers (Figure 1a), bilayers (Figure 1b), and under certain conditions, even trilayers of cylinders were observed on each sample (quantification *vide infra*). The regions with monolayers of PDMS cylinders, when plasma-treated, were converted into silica lines with pitch *L* and width *w* (Figure 1c−e). After plasma treatment of the bilayer regions, silica lines derived from the upper PDMS cylinders were deposited onto the substrate between silica structures from the lower layers. The resulting structure consisted of silica lines with a pitch of *L*/2 (Figure 1f−h). As can be seen in the scanning electron microscope (SEM) images in Figure 1h, silica lines originating from the upper PDMS cylinders had a rounder cross section. Identification of the silica lines derived from upper and lower PDMS cylinders was determined at sites of overlap and other defects (see Supporting Information, Figure S1).

Without process optimization, bilayer regions of PDMS cylinders generally produce SiO_x line arrays that have significant overlap between the lines that

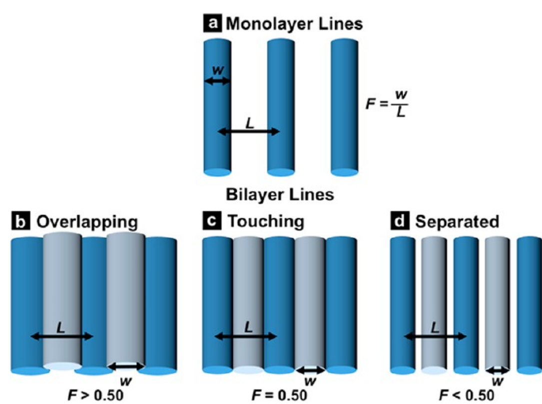

Figure 2. (a) Schematic representation of lines derived from a monolayer of cylinders. Fill ratio F is defined as the ratio of line width w to line pitch L, as measured in a monolayer region. (b–d) Assuming the simplest case where both top and bottom line widths are the same for bilayer lines, $F > 0.50$ results in bilayer lines that overlap (b); $F = 0.50$ results in lines that touch (c); and $F < 0.50$ results in lines that are separated (d).

originate from the upper and lower layers of PDMS cylinders, as shown schematically in Figure 1i and in the SEM images in Figure 1j,k. To attain the necessary control over line width to achieve sufficient separation of the SiO_x lines from the bilayer PS-*b*-PDMS system and form structures similar to those in Figure 1f, each of the processing parameters, including the solvent anneal conditions, the polymer film composition, the brush composition on the silicon surface, and the plasma conditions, were individually investigated. When these processing conditions were optimized, distinct silica lines were formed from both the upper and lower PDMS cylinders.

One important numerical parameter that describes the fraction of surface occupied by silica line features is the fill ratio F (*i.e.*, the line width w divided by the characteristic cylinder spacing L) as shown in Figure 2a. A fill ratio of 0.50 describes lines separated by spaces equal to the line width. If this fill ratio, $F = 0.50$, is observed in a region of SiO_x lines formed from a monolayer of PDMS cylinders, then lines formed from a bilayer of PDMS cylinders on the same sample will consist of silica lines in contact with one another, with no visible line separation and no overlap (Figure 2c). A fill ratio $F > 0.50$ observed in a monolayer region should correspond to bilayer regions where lines originating from the upper PDMS cylinders overlap with lines originating from the lower layer of PDMS cylinders (Figure 2b). Finally, a fill ratio $F < 0.50$ observed in a monolayer region would correspond to bilayer line patterns separated by distinct gaps (Figure 2d). It should be noted that these calculations apply to an ideal system, since it is assumed that silica lines originating from bilayer regions have the same L and w as those found in monolayer regions. In practice, while L remains the same, lines templated from the lower layer of bilayer cylinders tend to be wider than lines templated from the upper layer, and both tend to be wider than lines templated from a monolayer. In addition, as the fill ratio increased, line occlusion or contact between adjacent lines became more prevalent. Because line width measurements require both edges of a line to be visible, this occlusion and line contact prevented reliable measurements for samples with $F \geq 0.50$. Because of these challenges, initial process optimization was carried out on monolayer regions; the information learned from the monolayer optimization was then applied to the more challenging bilayer system. Unless otherwise stated, fill ratios, pitches and line widths were measured exclusively in regions of the substrate formed from monolayers of BCP cylinders. Our goal was a monolayer fill ratio of $F \leq 0.25$, which would then lead to bilayer lines separated by gaps as wide as the lines themselves; this goal may be overly ambitious, but was chosen to provide a buffer to accommodate for line waviness, differences in line widths, and other phenomena. A comparison of line analysis metrics for lines derived from both monolayers and bilayers of PS-*b*-PDMS is included in the Supporting Information (Figure S2).

The first and most obvious place to start the optimization is the annealing step, in which the self-assembly of these monolayers and bilayers of cylinders takes place. Thermal annealing could be used as a method to promote the self-assembly of horizontal cylinders. However, lines produced by this method had $F = 0.64 \pm 0.06$ (see Supporting Information, Figure S3), making them inferior to lines produced through solvent annealing. Thus, the solvent annealing process was used and monitored by *in situ* ellipsometry, with accompanying SEM imaging of the plasma-treated line structures. During a solvent anneal in THF vapor, solvent is absorbed by the BCP film, leading to significant increases in the film thickness. Figure 3a shows a typical curve describing the degree of swelling (D, calculated by dividing the measured *in situ* film thickness by the initial film thickness) of a PS-*b*-PDMS film at room temperature. As the solvent vapor infiltrates the polymer, the films initially swell rapidly before reaching a plateau. The rate at which the film swells is related to the volume and surface area of the solvent in the chamber, and also the ambient temperature, *via* their combined influence on the THF vapor pressure. Starting with an initial PS-*b*-PDMS film thickness of ~36 nm, the solvent vapor anneal was terminated at target degrees of swelling by quickly purging the chamber with air, which caused the swelled film to rapidly relax to its initial thickness and kinetically trap the self-assembled structures. Representative SEM images of SiO_x line structures obtained by terminating solvent anneals at different predetermined degrees of swelling are displayed in Figure 3b; all samples were plasma treated to convert the PDMS block to SiO_x and remove the PS before SEM

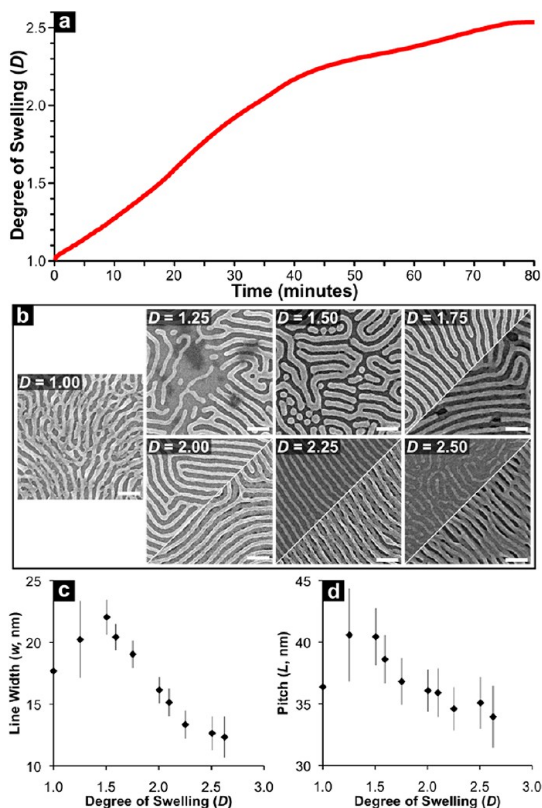

Figure 3. (a) Plot showing swelling of a 36 nm-thick neat PS-*b*-PDMS film throughout a typical 80 min solvent anneal (with tetrahydrofuran). (b) Representative SEM images of the plasma treated samples after stopping anneals at different degrees of swelling. Images that are split in half display monolayer regions in the top half, and bilayer regions in the bottom half, and all scale bars are 100 nm. (c, and d) Plots showing line width (c) and pitch (d) after swelling to different *D*. The error bars represent the standard deviation of all line width or pitch measurements that were made.

inspection. In the cases where the BCP films had formed regions of mono- and bilayers, two SEM images are shown, with the top left showing a monolayer region and the bottom right showing a bilayer region. The widths, *w*, and pitches, *L*, of monolayer line structures resulting from terminating the anneal at different degrees of swelling are plotted in Figure 3, panels c and d, respectively. Both line widths and pitch were observed to increase for $D \leq 1.50$, before slowly decreasing as the film continued to swell to $D = 2.63$. The initial increase in line width and pitch could be attributed to a gradual shift of polymer structures from their kinetically trapped as-cast state to a more thermodynamically favored state. Because insufficient solvent plasticizer was present early on, the initial reorganization was slow and nonuniform, as suggested by the large standard deviation in pitch and line width in the $D = 1.25$ samples. As the solvent content increased to $D \geq 1.50$, however, the mobility of the polymer became sufficient for the complete transition into organized parallel cylinders, and the standard deviation in cylinder pitch and width dropped markedly (Figure 3c,d). The steady decline of line width and pitch observed in these graphs was also observed by Jeong *et al.* in their solvent annealing work on the polymer P2VP-*b*-PDMS,[15] and was attributed to a solvent shielding effect, which lowers the effective χ parameter of the system. From the data shown in Figure 3, monolayer line widths varied during the course of the solvent anneal from 12 ± 2 to 22 ± 1 nm, and line pitch from 34 ± to 40 ± 2 nm. Despite the tendency toward reduced line widths with greater swelling, significant line overlap was still observed in all bilayer regions (monolayer *F* ranging from 0.54 ± 0.07 to 0.34 ± 0.07), and additional experimental refinements were required to form distinctly separated lines.

It has previously been shown that the addition of a homopolymer to a block copolymer film can effectively increase the pitch and the size of self-assembled domains.[46−48] In the present case, by adding PS homopolymer to form a PS/PS-*b*-PDMS blend, the ratio of PS:PDMS would increase and could enlarge the PS matrix interline spacing. Solutions of PS/PS-*b*-PDMS homopolymer blends were prepared with the homopolymer PS (10 kg/mol) content varying from 0 to 30 wt %. BCP films of these compositions with initial thicknesses of ∼36 nm were annealed in THF vapor to degrees of swelling, *D*, of 1.75, 2.00, and 2.25, and purged and plasma treated as described previously. SEM images of the self-assembled structures formed after swelling films to $D = 2.25$ are displayed in Figure 4a (see Supporting Information, Figures S5 and S6 for SEM images of $D = 1.75$ and 2.00). A slight tendency toward thinner and more widely spaced lines with higher PS homopolymer compositions can be observed; for example, in the case of $D = 2.25$, line widths of 13 ± 1 nm were reduced to 10 ± 1 nm (Figure 4b), and the pitch increased from 35 ± 2 to 38 ± 2 nm (Figure 4c) when a 25 wt % PS homopolymer blend was used. Both of these trends contributed to a decrease in fill ratio (*F*) from 0.38 ± 0.05 to 0.26 ± 0.04 (Figure 4d). In the final panel of Figure 4a at a homopolymer fraction of 30 wt %, the structures change drastically from line patterns to dot patterns, and this morphological change delineates the upper limit for PS homopolymer in the blend composition. Even at 25 wt %, the line structures displayed numerous defects, such as interruptions with areas of hexagonal dots and discontinuities. Similar trends were observed for $D = 1.75$ and $D = 2.00$ with respect to the pitch (Figure 4c), although the decrease in line width was not as pronounced and within the measured standard deviations (Figure 4b). It was concluded that a composition of 22.5 wt % PS/PS-*b*-PDMS would be applied to the bilayer system (*vide infra*) since it increased the pitch, reduced line width, and avoided the high level of defects observed at 25 wt % and 30 wt % PS.

As was noticed in the annealing experiments described in Figure 3, the silica lines derived from the

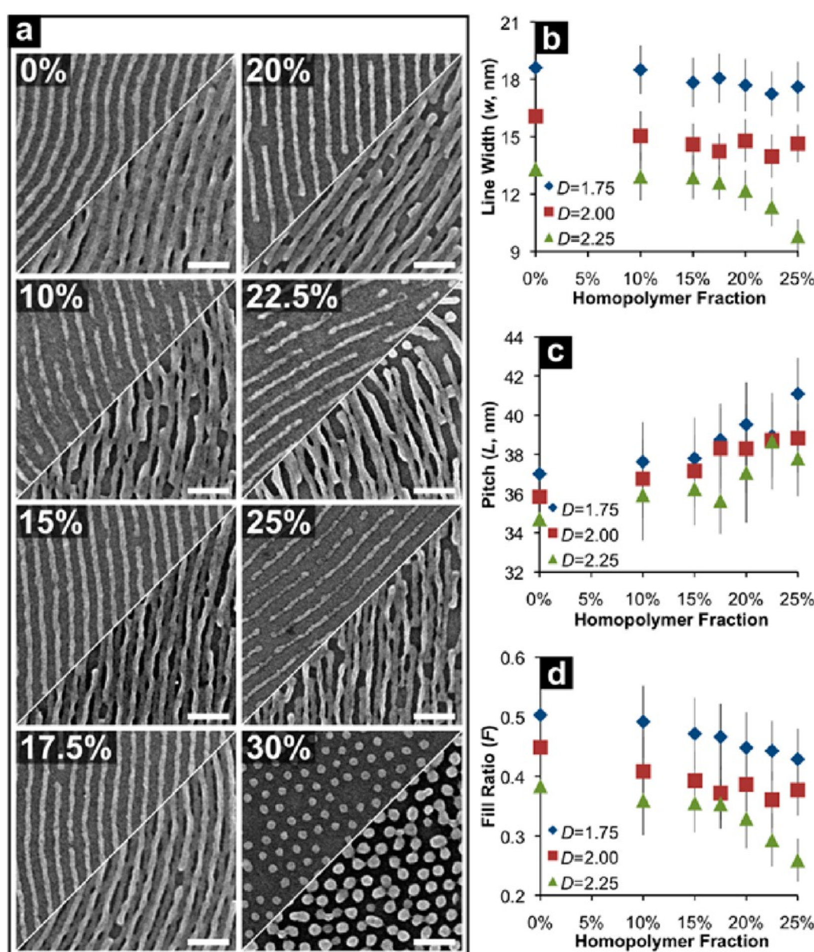

Figure 4. (a) SEM images demonstrating the evolution of structures swelled to a uniform D = 2.25 as the fraction of PS homopolymer in the films was increased. The top half of each image displays patterns found in monolayer regions, while the bottom half shows patterns found in bilayer regions, and all scale bars are 100 nm. (b−d) Plots of line width (b), pitch (c), and fill ratio (d) as the concentration of PS is increased up to 30 wt %. All samples have an initial film thickness of 36 nm. The error bars represent the standard deviation of all the line width or pitch measurements that were made.

lower level PDMS cylinders tended to be on average 2 to 3 nm wider than their upper level counterparts. For instance, for D = 2.25, the widths of lines derived from the upper and lower layer cylinders were 14 ± 1 nm and 16 ± 1 nm respectively. While one possible explanation was that these structures were exposed to the plasma longer and thus were etched to a greater extent, closer inspection from several cross-section and tilted SEM images also revealed that lines originating from lower layer cylinders were flat and spread over the wafer surface, suggesting possible interactions with the surface. To confirm this conjecture, PS and PDMS brush layers were grafted onto clean silicon substrates before the polymer films were spin-coated on the surface and solvent annealed. The addition of brush layers modifies the interfacial energy at the polymer-surface interface.[49] A thick coat of either hydroxy-terminated PS or PDMS was spin-coated on the silicon and heated in a vacuum oven at 130 °C for 2 h. The excess polymer was then rinsed off the silicon substrate with excess toluene, acetone, and isopropyl alcohol. The resulting thicknesses of these PDMS and PS brush layers were determined by ellipsometry and were found to be 2 and 5 nm, respectively. Thus, a BCP film normally 35 nm on the native silicon oxide was measured to be 37 nm when spin coated on a PDMS brush, or 40 nm when spin coated on a PS brush. A neat BCP film was spin-coated on the PS brush-coated surface and annealed in THF vapor to D = 2.00, and after plasma treatment, the structures derived from the monolayer and bilayer regions were compared to their analogs with only native oxide. In the plot in Figure 5, a very small reduction in line width was observed for the both the monolayer and bilayer lines, suggesting that the PS brush provided a small but measurable advantage with respect to the line width. In contrast, the PDMS brush yielded cylindrical lines that were always wider than their equivalents on native oxide or PS brushes. In the case where a PDMS brush was used, the line structures were partially obscured by a haze, likely of SiO_x, originating from the brush (see Figure 5f).

After optimizing for the annealing conditions, the film composition, and the interfacial properties with the PS brush, the next parameter to investigate was the

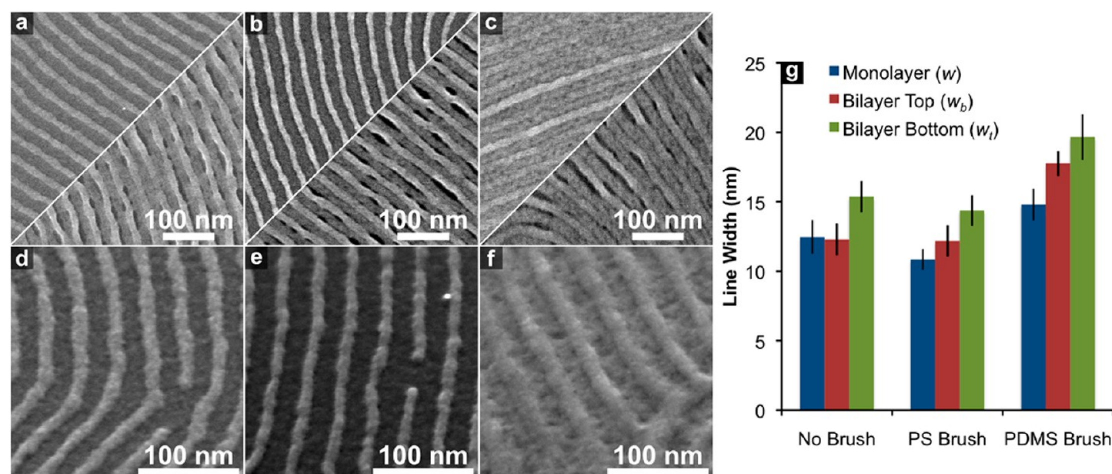

Figure 5. (a−f) SEM images of SiO_x line structures produced from solvent annealed PS-*b*-PDMS BCPs on Si wafers with no brush layer (a and d), PS brush layer (b and e), and PDMS brush layer (c and f). The measured initial thickness of these films including their brush layers were 35, 40, and 37 nm, respectively. In (a−c), regions with single layer lines are shown in the top left of each panel, and regions with double layers are shown in the bottom right. Close-up SEM images of the single-layer films tilted at 45° are displayed below for bare wafers (d), PS brush (e), and PDMS brush (f). (g) Graph of line widths measured from all samples.

plasma processing of annealed BCP films. Because the block copolymer films are capped with a surface PDMS layer at the BCP-air interface, an initial CF_4 plasma treatment to selectively etch the PDMS was required to allow access to the underlying self-assembled cylindrical structures.[50] Fixing the duration of this PDMS removal step at 10 s, the length of time of the subsequent O_2 plasma step to selectively etch the PS and convert the PDMS structures to SiO_x[24,51] was then varied on identically prepared samples (∼36 nm of the 22.5% PS blended film on a PS brush, swelled to $D = 2.00$). As the O_2 plasma exposure time was increased from 10 up to 30 s, the edges of the cylindrical structures, which were initially indistinct, became sharper and more well-defined, as shown in the images in Figure 6a. With increasing O_2 plasma time, however, these lines began to merge and by 50 s, the bilayer line structures consisted of large agglomerations of silica. Thus, after the initial 30 s of O_2 plasma treatment, no improvement in fill ratio was observed.

Another route to optimization of the plasma treatment was to use a plasma that more aggressively etched the PDMS cylinders to narrow the line widths, while simultaneously removing the PS matrix. Since O_2 and CF_4 plasmas selectively etch different BCP blocks, a plasma with tunable selectivity could be created from a combination of the two gases. In an attempt to find the ideal plasma composition and time, plasmas incorporating 10%, 20%, and 30% CF_4 were used, and SEM images of the resulting structures obtained from varying plasma exposure times are displayed in Figures 6b−d. As observed in these SEM images, an increase in plasma CF_4 content led to a decrease in line widths derived from both the upper and lower layers of PDMS cylinders, and thus there was a noticeable increase in the spacing between adjacent lines.

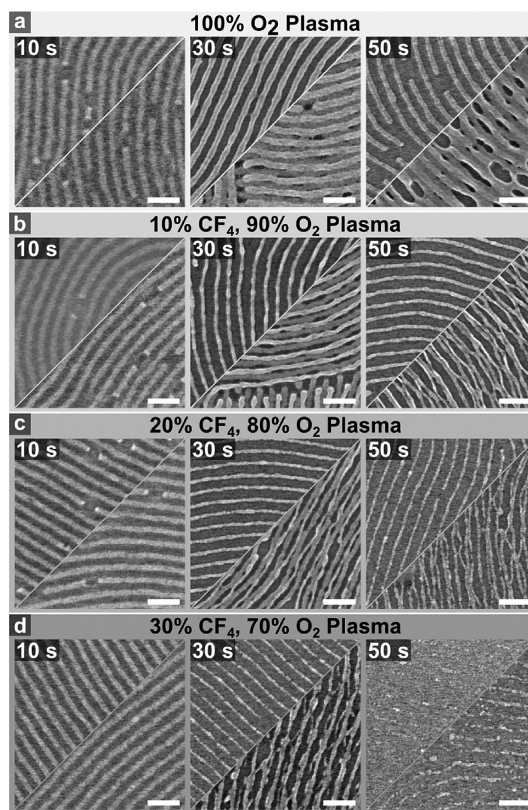

Figure 6. (a−d) The 22.5% PS blended samples swelled on a PS brush layer to $D = 2.00$, treated with 10 s of CF_4 plasma to remove the surface PDMS layer, and then subsequently subjected to 100% O_2 (a) or mixed O_2/CF_4 plasmas (b−d) for varying durations. The top halves of each image panel display monolayer regions, while the bottom halves display bilayer regions on the same sample. All scale bars are 100 nm.

As the concentration of CF_4 increased, however, the line width differences between the upper and lower lines also increased due to the fact that the upper lines

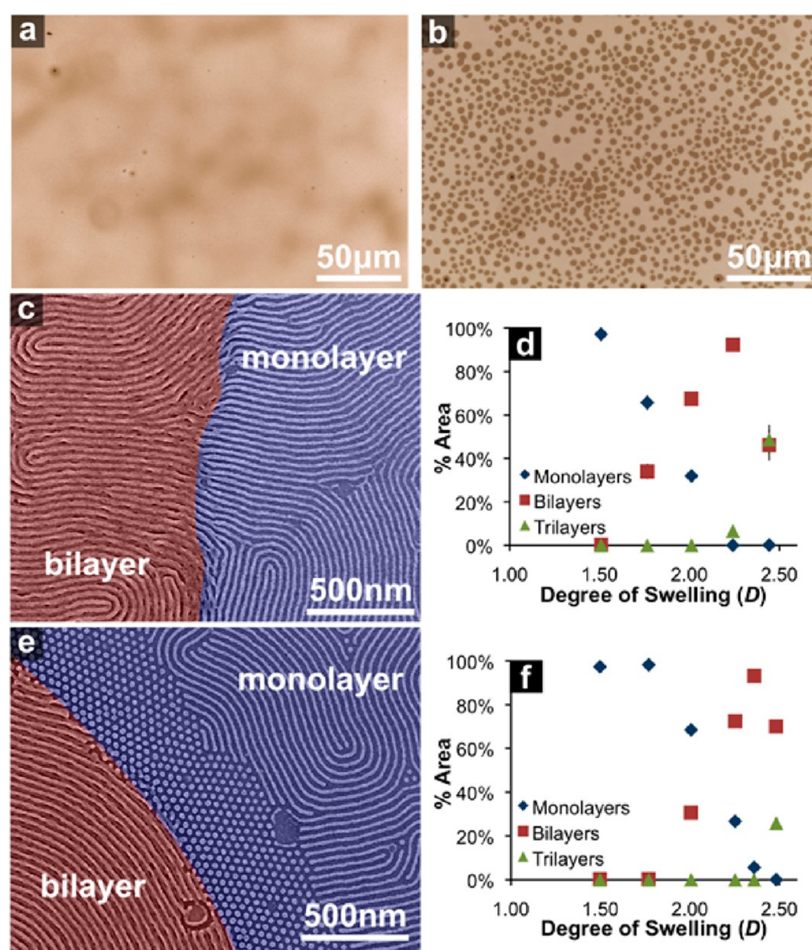

Figure 7. (a and b) Optical micrographs of neat BCP films swelled to $D = 1.25$ (a) and $D = 1.75$ (b). (c) SEM image showing the interface between monolayer and bilayer regions for neat PS-*b*-PDMS films. (d) Plot of the evolution of monolayer/bilayer/trilayer coverage with swelling, D, for neat PS-*b*-PDMS films with initial thickness of 36 nm (excluding the PS brush). (e) SEM image of the monolayer/bilayer interface within the 22.5% PS/PS-*b*-PDMS blended films. (f) Plot of the evolution of monolayer/bilayer/trilayer coverage with swelling, D, for 22.5% PS/PS-*b*-PDMS blended films with initial thickness of 36 nm.

were exposed to the etchant for longer periods of time. For example, a 20 s plasma exposure at 20% CF_4 produced top and bottom line widths of 14 ± 1 and 17 ± 1 nm, respectively, while an identical exposure in 30% CF_4 produced widths of 12 ± 1 and 16 ± 1 nm. As the plasma exposure times increased to 50 s or longer, individual lines began to deform and stick to adjacent lines. Thus, the plasma parameters had to be tuned such that enough CF_4 was present to increase the spacing without etching the top layers too quickly. For the 22.5% PS blended films, a 10% CF_4 plasma step for 25−30 s (Figure 6b) or a 20% CF_4 plasma step for 20−25 s gave optimum results (see Supporting Information, Figures S10 and S11, for additional images).

In addition to tuning the line width and pitch, it was also critical to control the percent coverage of monolayer and bilayer regions in the film on the microscale. To investigate the effect of film swelling on the fraction of monolayer and bilayer regions, neat BCP films of ~36 nm were spin coated on a PS brush-coated sample and annealed to different degrees of swelling, similar to the samples in Figure 3. Using optical microscopy, postanneal images of the films were taken at multiple locations on the sample. Because monolayer, bilayer, and even trilayer regions in the film have different thicknesses, these regions appeared in different colors under the optical microscope due to interference effects. The percent coverage of each of these regions was then determined for each sample using image processing (see Supporting Information for details) and displayed in Figure 7. Neat BCP films swelled to $D = 1.25$ showed some fluctuations in film thickness (Figure 7a), but discrete terraces were not observed until after $D > 1.50$ (Figure 7b). Upon closer inspection by SEM of the edges of these discrete terraces (Figure 7c), a clear transition from monolayer to bilayer lines was observed. As the films continued to swell, monolayer regions, which covered $97.2 \pm 0.4\%$ of the sample at $D = 1.50$, linearly gave way to bilayers until $D = 2.25$, when the distribution became $0.0 \pm 0.0\%$ monolayers, $92.4 \pm 0.8\%$ bilayers, and $6.6 \pm 0.4\%$ trilayers (Figure 7d). After this point, if the anneal was left to continue, bilayer regions began to convert into trilayer regions. Experiments performed for

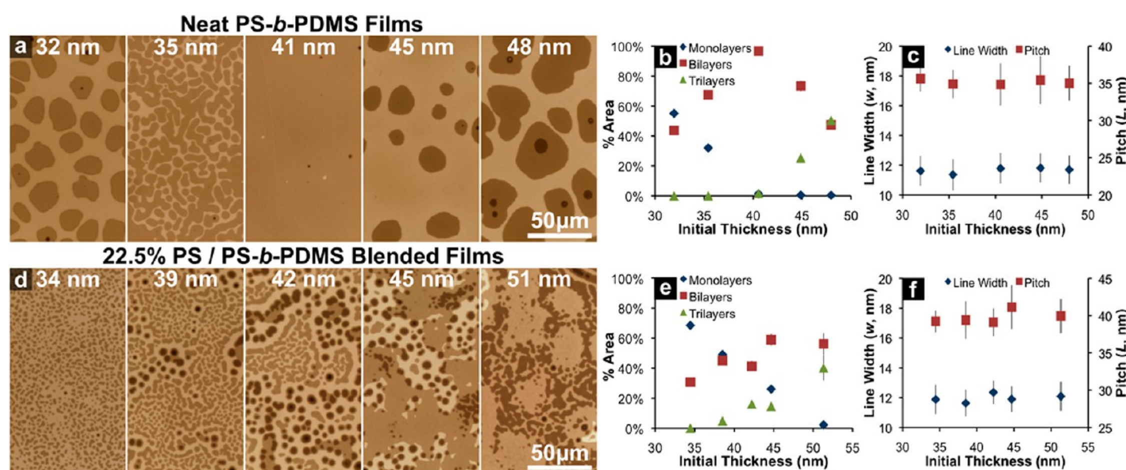

Figure 8. (a) Optical micrographs of neat PS-*b*-PDMS films on a PS brush with varying initial thicknesses swelled to D = 2.00. (b) Plot of the percent coverage of monolayer, bilayer, and trilayer regions in the same neat PS-*b*-PDMS samples. (c) Plot of line width and pitch of monolayers in these same neat PS-*b*-PDMS samples after a plasma treatment of 10% CF_4 for 25 s. (d) Optical micrographs of 22.5% PS/PS-*b*-PDMS blended films swelled to D = 2.00. (e) Plot of the percent coverage of monolayer, bilayer, and trilayer regions in the same 22.5% PS/PS-*b*-PDMS blended films. (f) Plot of line width and pitch of monolayers in these same PS blended samples after a plasma treatment of 10% CF_4 for 25 s.

the 22.5% PS blended films in identical conditions showed behavior similar to the neat BCP films with two key exceptions. First, inspection by SEM revealed a ~400–500 nm-wide strip of hexagonal PDMS dots at the boundary of monolayer/bilayer regions with 22.5% PS (Figure 7e). One possible explanation for the presence of the dot interface at the boundaries is that the film thicknesses fall between that of the monolayer and bilayer regions, and that these local film thicknesses favor the local formation of spherocylinders,[52] which are converted into dot patterns upon exposure to plasma. These dot patterns were not observed in the neat films likely because this phase does not exist at the higher PDMS volume fraction (f_{PDMS} ~ 0.34 for neat films, ~ 0.26 for 22.5% PS blended films). Second, unlike the swelling of neat BCP films, the monolayer regions did not begin to transform into bilayers until after D = 1.75 (Figure 7f). After D = 1.75, the monolayers continued to convert into bilayer regions until at D = 2.36, where the bilayer fraction peaked at 93.2 ± 2.1%, with 5.6 ± 1.6% monolayers and 0.0 ± 0.0% trilayers.

Although the degree of swelling, D, clearly had an effect on the percent coverage of these layered structures in the film, it was not a useful parameter to tune the coverage of bilayer regions, as it also had great influence over line widths and pitch. An alternative parameter was the initial film thickness. As shown in Figure 8, neat BCP films were deposited at various thicknesses (from 32 to 48 nm) onto a PS brush coated sample and annealed to a fixed degree of swelling of D = 2.00. The resulting terrace structures displayed in Figure 8a clearly demonstrate that the monolayer, bilayer, and trilayer fractions of a film can be tuned by varying the initial film thickness. As shown in Figure 8b, an initial thickness of ~41 nm produced monolayer, bilayer, and trilayer area fractions of 1.3 ± 0.9%, 96.7 ± 0.8%, and 1.7 ± 0.4%, respectively. Thus, near-uniform bilayers can be attained across the entire sample if a film of ~41 nm is swelled to a degree of swelling of D = 2.00. When these films were subjected to identical and optimized (10% CF_4 for 25 s in the second step) plasma conditions, no obvious relationship between the initial film thickness and the width or pitch of these lines was observed (Figure 8c); the decoupling of these parameters is important, since it means that initial film thickness can be independently varied to optimize for bilayer formation, without affecting line width and pitch. As shown in the optical micrographs in Figure 8d, 22.5% PS blended films behaved quite differently than their neat BCP counterparts. Trilayer regions started appearing and growing before all the monolayer regions were eliminated (Figure 8d). One consequence of this early onset of trilayers is that although 22.5% PS blended films can produce line arrays at lower F than neat BCP films, it is impossible to have high percentage coverage of bilayer regions. SEM images of these films (Figure 8e) also showed that the initial film thickness had no obvious effect on line width or pitch.

The optimized processing conditions can also be utilized for graphoepitaxy applications in which morphological features assist in guiding the self-assembly of polymers to produce patterns with long-range order, as demonstrated in Figure 9 (and Supporting Information Figures S14 and S15). The guiding features were formed through electron beam lithography with the negative photoresist HSQ. Graphoepitaxy was found to be effective in directing the alignment of the densely packed silica lines for both neat BCP films and also 22.5% PS blended films on a PS brush layer. As shown in Figure 9, a 22.5% PS/PS-*b*-PDMS blend was swelled to D = 2.00 and subjected to a 10%

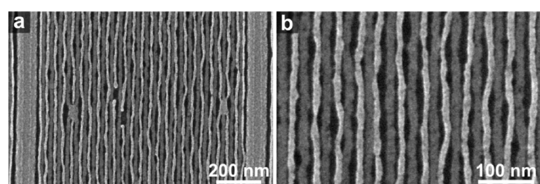

Figure 9. (a) SEM image of ordered double-layer structures along graphoepitaxial features that are spaced approximately 1 μm apart and patterned by electron beam lithography. A 22.5% PS/PS-*b*-PDMS blend was swelled to D = 2.00 on a PS brush and subject to a 25 s 10% CF_4 plasma step. (b) Close-up of the top right corner of the SEM image (a).

CF_4 plasma step for 25 s. The resulting densely packed lines had a bilayer pitch of 19 $\pm$ 2 nm, and widths of 10 $\pm$ 1 and 14 $\pm$ 1 nm for the silica lines derived from the upper and lower layer cylinders, respectively. While the goal, as stated early on, had been F = 0.25, optimization of the experimental conditions resulted in, in this case, F = 0.27 $\pm$ 0.05.

There is considerable room for improvement with respect to control over the resulting lines produced through the use of bilayer-based BCP films, particularly with regards to line edge roughness (LER) and related parameters. As can be seen from the SEM images in Figure 1, the monolayer cylinders are smoother, and have obvious lower peristaltic line edge roughness. The silica lines derived from the bilayer PS-*b*-PDMS structures present considerable undulations, and will require careful optimization to improve the LER.[53] One possible source of the observed undulations includes the melting or flowing of PDMS cylinders (melting point ~ -50 °C)[54] if the supporting PS underlayer degrades during the plasma treatment before the PDMS fully converts into silica. Solutions to this problem could include adding groups to cross-link the PDMS prior to plasma treatment, or using anisotropic plasma etching conditions to prevent the underlying PS from degrading from underneath the cylinders before they become silica.[55] The relaxation step, where solvent vapor is rapidly removed from the sample chamber, may also play a role in kinetically trapping or even resulting in undulations; a possible solution could be a gentle secondary thermal anneal.[56] In addition, placement accuracy will also need to be thoroughly investigated with respect to graphoepitaxy and the use of registration marks, as has recently been carried out by Doerk and co-workers.[57] One particularly promising direction to improving LER is to reduce the interfacial tension between the two blocks through the addition of a third nonvolatile component as a `compatibilizer' to lower the surface energy at the interfaces in these nanoscale phase segregated phases.[58] The second direction for attention is the plasma conversion step—the transformation of flexible PDMS into a brittle and fragile metal oxide (in this case, silica) locks in the resulting specific shape under these low temperature conditions. Thus, silica precursors may not be the ideal material to produce lines with low LER when compared with flexible organic, and possibly even metallic precursors that are more readily annealed. These aspects will be the focus of upcoming work.

CONCLUSIONS

Utilizing films of bilayer PS-*b*-PDMS cylindrical assemblies as templates, it was possible to generate closely spaced SiO_x line patterns on a silicon substrate. By tuning the degree of swelling and/or blending the BCP film with PS homopolymer, it was possible to reduce the width and tune the pitch of these silica lines. The line widths of these structures could then be more finely tuned by adjusting a number of other parameters, including the brush layer and the duration/composition of the plasma treatment. If 22.5% PS blended films are used, the monolayer fill ratio could be reduced to F = 0.27 $\pm$ 0.05. The coverage of bilayer regions across a sample, on the multimicrometer scale, could then be tuned by adjusting the initial thickness of the BCP film prior to swelling. Thus, a PS-*b*-PDMS polymer that normally produces monolayer silica lines with a pitch of ~36 nm can be used to create denser line arrays at a pitch of 18 nm with bilayer coverage as high as 96.7 $\pm$ 0.8%. The system is not yet fully optimized with respect to line edge roughness, control over relative line heights, and other factors, but there remain other parameters for optimization, including additives to the PS-*b*-PDMS BCP and BCP blends, further optimization of plasma conditions, and different anneals.

METHODS

Materials and Cleaning Procedures. Concentrated HCl (aq), NH_4OH (aq) and tetramethylammonium hydroxide (TMAH) were obtained from J. T. Baker; H_2O_2 was obtained from Fisher Scientific; heptane, tetrahydrofuran (THF), and toluene were obtained from Caledon Laboratories Ltd.; PS-*b*-PDMS, OH-terminated PS and PDMS homopolymers were obtained from Polymer Source, Inc.; methyl isobutyl ketone (MIBK) was obtained from MicroChem; hydrogen silsesquioxane (HSQ) was obtained from Dow Corning; and silicon wafers were obtained from University Wafer. Prime grade 100 mm n-type silicon (100) wafers were diced into 1 cm × 1 cm squares using a Disco DAD 321 dicing saw. These silicon squares were degreased in an ultrasonic bath with methanol for 15 min and dried in a stream of nitrogen gas. Following RCA cleaning procedures,[59] the silicon squares were first immersed in an RCA I cleaning solution [1:1:6 solution of 30% NH_4OH (aq), 30% H_2O_2 (aq), and 18 $\Omega \cdot$cm deionized water] at 80 °C for 15 min, and then an RCA II cleaning solution [1:1:5 solution of 38% HCl (aq), 30% H_2O_2 (aq), and 18 $\Omega \cdot$cm deionized water] at 80 °C for 15 min before being thoroughly rinsed with water and dried in a nitrogen stream.

Fabrication of Wall Features for Graphoepitaxy. A 6% solution of HSQ in MIBK (XR-1541) was diluted in a 1:5 volume ratio with

MIBK to create a 1% HSQ solution. The diluted solution was spin coated at 3000 rpm for 30 s and then baked on a hot plate at 100 °C for 15 min. The samples were then loaded into a RAITH 150-2 electron beam lithography system to write wall features for directed self-assembly. After exposure, the patterns were developed by immersion in a 25% aqueous solution of TMAH for 30 s, followed by a rinse with distilled water.

Brush Layers. To deposit PS brushes, 15 μL of a 2 wt % solution of hydroxyl-terminated polystyrene (PS−OH, M_n = 10 000 g/mol) in toluene was spin-coated on a clean silicon square at 2000 rpm for 40 s. The resulting thin film sample was then placed inside a vacuum oven and heated at 130 °C for 2 h. The unreacted PS was then removed from the sample with a rinse of acetone followed by isopropyl alcohol. For PDMS brushes, the same procedure was used except a 2 wt % heptane solution of hydroxyl-terminated polydimethylsiloxane (PDMS−OH, M_n = 5000 g/mol) was substituted. Contact angles with deionized water were 4° for freshly cleaned samples, 90° for samples with grafted PS brushes, and 104° for samples with grafted PDMS brushes.

Block Copolymer Self-Assembly. The 1.2 wt % solutions of the PS-*b*-PDMS block copolymer ($M_{n,PS}$ = 31 000 g/mol, $M_{n,PDMS}$ = 14 500 g/mol) in toluene were spin-coated onto clean or brush-coated Si substrates at 4000 rpm for 40 s. For the BCP-homopolymer blends, a 1.2 wt % solution of the brush polystyrene homopolymer[35] in toluene was mixed with the PS-*b*-PDMS solution at the ratios noted. The resulting films were then placed in a custom solvent anneal chamber to allow monitoring of the film swelling using an L116S ellipsometer from Gaertner Scientific during the annealing process. One milliliter of THF was then deposited in a well inside the chamber, and the chamber was sealed. Once the desired swelling ratio was reached, the chamber was opened and immediately purged with air to rapidly relax the swelled film to its original thickness (<1 s). The kinetically trapped film was then transferred to a Plasmalab μEtch reactive ion etcher for two steps of plasma etching. Unless otherwise noted, the first step used 100 mTorr of CF_4 at 50 W RF power for 10 s, and this was immediately followed by the second step using 100 mTorr of O_2 at 30 W RF power for 30 s. Scanning electron microscope (SEM) images of all samples were acquired using a Hitachi S-4800 SEM.

Image Analysis. SEM images taken of line structures using the Hitachi S-4800 were analyzed using a Quartz PCI Imaging program. Line widths were measured manually 20−30 times at different positions in each image by dragging the line tool from one edge of the line to other. Similarly, the pitch was measured by dragging the cursor from the left edge of one line to the left edge of an adjacent line. This process was repeated for 2 to 3 images in different locations on each sample at 100 000× magnification.

The bilayer coverage of a sample was measured by taking 200× optical microscopy images from 5 distinct regions in each sample. The images were then converted to grayscale images and analyzed in ImageJ.[60] Through multiple uses of the threshold function, each pixel was mapped according to the number of BCP layers the film incorporates at that position. The fraction of pixels with each BCP layer count was then calculated, and by averaging the pixel counts from multiple areas, the BCP layer coverage of each sample was determined. For a more detailed procedure, please see the Supporting Information (Figure S13).

Conflict of Interest: The authors declare no competing financial interest.

Supporting Information Available: Scanning electron micrographs, graphs, line measurement details, solvent anneal details, plasma details, and image processing details. This material is available free of charge *via* the Internet at http://pubs.acs.org.

Acknowledgment. This work was supported by NSERC, Alberta Innovates Technology Futures, and NRC-NINT. The authors thank the University of Alberta NanoFab for both clean room and e-beam lithography support. The authors also thank Jeffrey N. Murphy and Andrew Wong for their development of software to facilitate the creation of BCP swelling curves.

REFERENCES AND NOTES

1. Darling, S. B. Directing the Self-Assembly of Block Copolymers. *Prog. Polym. Sci.* **2007**, *32*, 1152–1204.
2. Bang, J.; Jeong, U.; Ryu, D. Y.; Russell, T. P.; Hawker, C. J. Block Copolymer Nanolithography: Translation of Molecular Level Control to Nanoscale Patterns. *Adv. Mater.* **2009**, *21*, 4769–4792.
3. Kim, H.-C.; Park, S.-M.; Hinsberg, W. D. Block Copolymer Based Nanostructures: Materials, Processes, and Applications to Electronics. *Chem. Rev.* **2010**, *110*, 146–177.
4. Schacher, F. H.; Rupar, P. A.; Manners, I. Functional Block Copolymers: Nanostructured Materials with Emerging Applications. *Angew. Chem., Int. Ed.* **2012**, *51*, 7898–7921.
5. Albert, J. N. L.; Bogart, T. D.; Lewis, R. L.; Beers, K. L.; Fasolka, M. J.; Hutchison, J. B.; Vogt, B. D.; Epps, T. H. Gradient Solvent Vapor Annealing of Block Copolymer Thin Films Using a Microfluidic Mixing Device. *Nano Lett.* **2011**, *11*, 1351–1357.
6. Marencic, A. P.; Register, R. A. Controlling Order in Block Copolymer Thin Films for Nanopatterning Applications. *Annu. Rev. Chem. Biomol. Eng.* **2010**, *1*, 277–297.
7. Galatsis, K.; Wang, K. L.; Ozkan, M.; Ozkan, C. S.; Huang, Y.; Chang, J. P.; Monbouquette, H. G.; Chen, Y.; Nealey, P.; Botros, Y. Patterning and Templating for Nanoelectronics. *Adv. Mater.* **2010**, *22*, 769–778.
8. Black, C. T.; Ruiz, R.; Breyta, G.; Cheng, J. Y.; Colburn, M. E.; Guarini, K. W.; Kim, H.-C.; Zhang, Y. Polymer Self-Assembly in Semiconductor Microelectronics. *IBM J. Res. Dev.* **2007**, *51*, 605–633.
9. Bates, F.; Fredrickson, G. Block Copolymer Thermodynamics—Theory and Experiment. *Annu. Rev. Phys. Chem.* **1990**, *41*, 525–557.
10. Park, S.; Lee, D. H.; Xu, J.; Kim, B.; Hong, S. W.; Jeong, U.; Xu, T.; Russell, T. P. Macroscopic 10-Terabit-per-Square-Inch Arrays from Block Copolymers with Lateral Order. *Science* **2009**, *323*, 1030–1033.
11. Liu, G.; Stoykovich, M. P.; Ji, S.; Stuen, K. O.; Craig, G. S. W.; Nealey, P. F. Phase Behavior and Dimensional Scaling of Symmetric Block Copolymer−Homopolymer Ternary Blends in Thin Films. *Macromolecules* **2009**, *42*, 3063–3072.
12. Poelma, J. E.; Ono, K.; Miyajima, D.; Aida, T.; Satoh, K.; Hawker, C. J. Cyclic Block Copolymers for Controlling Feature Sizes in Block Copolymer Lithography. *ACS Nano* **2012**, *6*, 10845–10854.
13. Cushen, J. D.; Bates, C. M.; Rausch, E. L.; Dean, L. M.; Zhou, S. X.; Willson, C. G.; Ellison, C. J. Thin Film Self-Assembly of Poly(trimethylsilylstyrene-*b*-D,L-lactide) with Sub-10 nm Domains. *Macromolecules* **2012**, *45*, 8722–8728.
14. Runge, M. B.; Bowden, N. B. Synthesis of High Molecular Weight Comb Block Copolymers and Their Assembly into Ordered Morphologies in the Solid State. *J. Am. Chem. Soc.* **2007**, *129*, 10551–10560.
15. Jeong, J. W.; Park, W. I.; Kim, M.-J.; Ross, C. A.; Jung, Y. S. Highly Tunable Self-Assembled Nanostructures from a Poly(2-vinylpyridine-*b*-dimethylsiloxane) Block Copolymer. *Nano Lett.* **2011**, *11*, 4095–4101.
16. Paik, M. Y.; Bosworth, J. K.; Smilges, D.-M.; Schwartz, E. L.; Andre, X.; Ober, C. K. Reversible Morphology Control in Block Copolymer Films *via* Solvent Vapor Processing: An in Situ GISAXS Study. *Macromolecules* **2010**, *43*, 4253–4260.
17. Liu, C.-C.; Ramírez-Hernández, A.; Han, E.; Craig, G. S. W.; Tada, Y.; Yoshida, H.; Kang, H.; Ji, S.; Gopalan, P.; de Pablo, J. J.; *et al.* Chemical Patterns for Directed Self-Assembly of Lamellae-Forming Block Copolymers with Density Multiplication of Features. *Macromolecules* **2013**, *46*, 1415–1424.
18. Jung, Y. S.; Chang, J. B.; Verploegen, E.; Berggren, K. K.; Ross, C. A. A Path to Ultranarrow Patterns Using Self-Assembled Lithography. *Nano Lett.* **2010**, *10*, 1000–1005.
19. Cushen, J. D.; Otsuka, I.; Bates, C. M.; Halila, S.; Fort, S.; Rochas, C.; Easley, J. A.; Rausch, E. L.; Thio, A.; Borsali, R.; *et al.* Oligosaccharide/Silicon-Containing Block Copolymers with 5 nm Features for Lithographic Applications. *ACS Nano* **2012**, *6*, 3424–3433.

20. Bates, C. M.; Seshimo, T.; Maher, M. J.; Durand, W. J.; Cushen, J. D.; Dean, L. M.; Blachut, G.; Ellison, C. J.; Willson, C. G. Polarity-Switching Top Coats Enable Orientation of Sub-10-nm Block Copolymer Domains. *Science* **2012**, *338*, 775–779.
21. Ruiz, R.; Dobisz, E.; Albrecht, T. R. Rectangular Patterns Using Block Copolymer Directed Assembly for High Bit Aspect Ratio Patterned Media. *ACS Nano* **2011**, *5*, 79–84.
22. Naito, K.; Hieda, H.; Sakurai, M.; Kamata, Y.; Asakawa, K. 2.5-Inch Disk Patterned Media Prepared by an Artificially Assisted Self-Assembling Method. *IEEE Trans. Magn.* **2002**, *38*, 1949–1951.
23. Thurn-Albrecht, T.; Schotter, J.; Kästle, G. A.; Emley, N.; Shibauchi, T.; Krusin-Elbaum, L.; Guarini, K.; Black, C. T.; Tuominen, M. T.; Russell, T. P. Ultrahigh-Density Nanowire Arrays Grown in Self-Assembled Diblock Copolymer Templates. *Science* **2000**, *290*, 2126–2129.
24. Park, W. I.; You, B. K.; Mun, B. H.; Seo, H. K.; Lee, J. Y.; Hosaka, S.; Yin, Y.; Ross, C. A.; Lee, K. J.; Jung, Y. S. Self-Assembled Incorporation of Modulated Block Copolymer Nanostructures in Phase-Change Memory for Switching Power Reduction. *ACS Nano* **2013**, *7*, 2651–2658.
25. Black, C. T. Self-Aligned Self-Assembly of Multi-Nanowire Silicon Field Effect Transistors. *Appl. Phys. Lett.* **2005**, *87*, 163116.
26. Chang, L.-W.; Wong, H.-S. P. Diblock Copolymer Directed Self-Assembly for CMOS Device Fabrication. *Proc. SPIE* **2006**, *6156*, 615611−1–615611−6.
27. Li, W.; Yang, S. Creation of Sub-20-nm Contact Using Diblock Copolymer on a 300 nm Wafer for Complementary Metal Oxide Semiconductor Applications. *J. Vac. Sci. Technol., B* **2007**, *25*, 1982–1984.
28. Arnold, M.; Cavalcanti-Adam, E. A.; Glass, R.; Blümmel, J.; Eck, W.; Kantlehner, M.; Kessler, H.; Spatz, J. P. Activation of Integrin Function by Nanopatterned Adhesive Interfaces. *ChemPhysChem* **2004**, *5*, 383–388.
29. Walter, N.; Selhuber, C.; Kessler, H.; Spatz, J. P. Cellular Unbinding Forces of Initial Adhesion Processes on Nanopatterned Surfaces Probed with Magnetic Tweezers. *Nano Lett.* **2006**, *6*, 398–402.
30. Welander, A. M.; Kang, H.; Stuen, K. O.; Solak, H. H.; Müller, M.; de Pablo, J. J.; Nealey, P. F. Rapid Directed Assembly of Block Copolymer Films at Elevated Temperatures. *Macromolecules* **2008**, *41*, 2759–2761.
31. Zhang, X.; Harris, K. D.; Wu, N. L. Y.; Murphy, J. N.; Buriak, J. M. Fast Assembly of Ordered Block Copolymer Nanostructures through Microwave Annealing. *ACS Nano* **2010**, *4*, 7021–7029.
32. Zhang, X.; Murphy, J. N.; Wu, N. L. Y.; Harris, K. D.; Buriak, J. M. Rapid Assembly of Nanolines with Precisely Controlled Spacing from Binary Blends of Block Copolymers. *Macromolecules* **2011**, *44*, 9752–9757.
33. Stoykovich, M. P.; Muller, M.; Kim, S. O.; Solak, H. H.; Edwards, E. W.; de Pablo, J. J.; Nealey, P. F. Directed Assembly of Block Copolymer Blends into Nonregular Device-Oriented Structures. *Science* **2005**, *308*, 1442–1446.
34. Stoykovich, M. P.; Kang, H.; Daoulas, K. C.; Liu, G.; Liu, C.-C.; de Pablo, J. J.; Müller, M.; Nealey, P. F. Directed Self-Assembly of Block Copolymers for Nanolithography: Fabrication of Isolated Features and Essential Integrated Circuit Geometries. *ACS Nano* **2007**, *1*, 168–175.
35. Liu, G.; Thomas, C. S.; Craig, G. S. W.; Nealey, P. F. Integration of Density Multiplication in the Formation of Device-Oriented Structures by Directed Assembly of Block Copolymer−Homopolymer Blends. *Adv. Funct. Mater.* **2010**, *20*, 1251–1257.
36. Kang, H.; Craig, G. S. W.; Nealey, P. F. Directed Assembly of Asymmetric Ternary Block Copolymer-homopolymer Blends Using Symmetric Block Copolymer into Checkerboard Trimming Chemical Pattern. *J. Vac. Sci. Technol., B* **2008**, *26*, 2495.
37. Yang, J. K. W.; Jung, Y. S.; Chang, J.-B.; Mickiewicz, R. A.; Alexander-Katz, A.; Ross, C. A.; Berggren, K. K. Complex Self-Assembled Patterns Using Sparse Commensurate Templates with Locally Varying Motifs. *Nat. Nanotechnol.* **2010**, *5*, 256–260.
38. Tavakkoli, K. G., A.; Gotrik, K. W.; Hannon, A. F.; Alexander-Katz, A.; Ross, C. A.; Berggren, K. K. Templating Three-Dimensional Self-Assembled Structures in Bilayer Block Copolymer Films. *Science* **2012**, *336*, 1294–1298.
39. Wu, N. L. Y.; Zhang, X.; Murphy, J. N.; Chai, J.; Harris, K. D.; Buriak, J. M. Density Doubling of Block Copolymer Templated Features. *Nano Lett.* **2011**, *12*, 264–268.
40. Cochran, E. W.; Morse, D. C.; Bates, F. S. Design of ABC Triblock Copolymers Near the ODT with the Random Phase Approximation. *Macromolecules* **2003**, *36*, 782–792.
41. Dai, K. H.; Kramer, E. J. Determining the Temperature-Dependent Flory Interaction Parameter for Strongly Immiscible Polymers from Block Copolymer Segregation Measurements. *Polymer* **1994**, *35*, 157–161.
42. Jung, G.-Y.; Li, Z.; Wu, W.; Chen, Y.; Olynick, D. L.; Wang, S.-Y.; Tong, W. M.; Williams, R. S. Vapor-Phase Self-Assembled Monolayer for Improved Mold Release in Nanoimprint Lithography. *Langmuir* **2005**, *21*, 1158–1161.
43. Lowe, R. D.; Pellow, M. A.; Stack, T. D. P.; Chidsey, C. E. D. Deposition of Dense Siloxane Monolayers from Water and Trimethoxyorganosilane Vapor. *Langmuir* **2011**, *27*, 9928–9935.
44. Diebold, R. M.; Clarke, D. R. Smooth, Aggregate-Free Self-Assembled Monolayer Deposition of Silane Coupling Agents on Silicon Dioxide. *Langmuir* **2012**, *28*, 15513–15520.
45. Burgess, I. B.; Koay, N.; Raymond, K. P.; Kolle, M.; Lončar, M.; Aizenberg, J. Wetting in Color: Colorimetric Differentiation of Organic Liquids with High Selectivity. *ACS Nano* **2012**, *6*, 1427–1437.
46. Peng, J.; Gao, X.; Wei, Y.; Wang, H.; Li, B.; Han, Y. Controlling the Size of Nanostructures in Thin Films *via* Blending of Block Copolymers and Homopolymers. *J. Chem. Phys.* **2005**, *122*, 114706.
47. Jeong, U.; Kim, H. -C; Rodriguez, R. L.; Tsai, I. Y.; Stafford, C. M.; Kim, J. K.; Hawker, C. J.; Russell, T. P. Asymmetric Block Copolymers with Homopolymers: Routes to Multiple Length Scale Nanostructures. *Adv. Mater.* **2002**, *14*, 274–276.
48. Winey, K. I.; Thomas, E. L.; Fetters, L. J. Swelling of Lamellar Diblock Copolymer by Homopolymer: Influences of Homopolymer Concentration and Molecular Weight. *Macromolecules* **1991**, *24*, 6182–6188.
49. Mansky, P.; Liu, Y.; Huang, E.; Russell, T. P.; Hawker, C. Controlling Polymer-Surface Interactions with Random Copolymer Brushes. *Science* **1997**, *275*, 1458–1460.
50. Jung, Y. S.; Ross, C. A. Orientation-Controlled Self-Assembled Nanolithography Using a Polystyrene−Polydimethylsiloxane Block Copolymer. *Nano Lett.* **2007**, *7*, 2046–2050.
51. Hillborg, H.; Ankner, J. F.; Gedde, U. W.; Smith, G. D.; Yasuda, H. K.; Wikström, K. Crosslinked Polydimethylsiloxane Exposed to Oxygen Plasma Studied by Neutron Reflectometry and Other Surface Specific Techniques. *Polymer* **2000**, *41*, 6851–6863.
52. Li, W.; Liu, M.; Qiu, F.; Shi, A.-C. Phase Diagram of Diblock Copolymers Confined in Thin Films. *J. Phys. Chem. B* **2013**, *117*, 5280–5288.
53. Stoykovich, M. P.; Daoulas, K. C.; Müller, M.; Kang, H.; de Pablo, J. J.; Nealey, P. F. Remediation of Line Edge Roughness in Chemical Nanopatterns by the Directed Assembly of Overlying Block Copolymer Films. *Macromolecules* **2010**, *43*, 2334–2342.
54. Andrianov, K. A.; Slonimskiĭ, G. L.; Zhdanov, A. A.; Yu. Levin, V.; Godovskiĭ, Y. K.; Moskalenko, V. A. Some Physical Properties of Polyorganosiloxanes. I. Linear Polyorganosiloxanes. *J. Polym. Sci., Part A-1: Polym. Chem.* **1972**, *10*, 1–22.
55. Mansano, R. D.; Verdonck, P.; Maciel, H. S. Anisotropic Reactive Ion Etching in Silicon, Using a Graphite Electrode. *Sensors Actuators Phys* **1998**, *65*, 180–186.
56. Kim, E.; Ahn, H.; Park, S.; Lee, H.; Lee, M.; Lee, S.; Kim, T.; Kwak, E.-A.; Lee, J. H.; Lei, X.; *et al.* Directed Assembly of High Molecular Weight Block Copolymers: Highly Ordered

Line Patterns of Perpendicularly Oriented Lamellae with Large Periods. *ACS Nano* **2013**, *7*, 1952–1960.
57. Doerk, G. S.; Liu, C.-C.; Cheng, J. Y.; Rettner, C. T.; Pitera, J. W.; Krupp, L. E.; Topuria, T.; Arellano, N.; Sanders, D. P. Pattern Placement Accuracy in Block Copolymer Directed Self-Assembly Based on Chemical Epitaxy. *ACS Nano* **2013**, *7*, 276–285.
58. Fang, L.; Wei, M.; Shang, Y.; Kazmer, D.; Barry, C.; Mead, J. Precise Pattern Replication of Polymer Blends into Non-uniform Geometries *via* Reducing Interfacial Tension Between Two Polymers. *Langmuir* **2012**, *28*, 10238–10245.
59. Kern, W. *Handbook of Semiconductor Wafer Cleaning Technology: Science, Technology, and Applications*; Noyes Publications: Park Ridge, NJ, 1993.
60. Rasband, W. S. *ImageJ*; U. S. National Institutes of Health: Bethesda, MD, 1997.